Journal of Chemical Health Risks

www.jchr.org

JCHR (2019) 9(4), 398-408 | ISSN:2251-6727

Unlocking the Potential of Copper Substituted Nickel Maganite Spinels for High-Performance Ammonia Gas Sensor.

U. D. Kadam, S. M. Arde, B. S. Shirke, R. S. Pandav*

Department of Chemistry, Yashwantrao Chavan Warana Mahavidyalaya, Warananagar 416 113, Maharashtra, India. (02328)224041.

*Corresponding Author: Email- rajkumarpandav@gmail.com

Contributing author e-mails: uttamkadam123@gmail.com, satyanarayan.arde2520@gmail.com, bss_chemistry@yahoo.com

(**Received**: 14 December 2018 **Revised**: 01 January 2019 **Accepted**: 18 February 2019)

KEYWORDS

Sol-gel synthesis, copper substituted nickel manganite, nanoparticles, catalyst, pollutant, biota, ammonia gas sensing.

ABSTRACT:

Nanocrystalline powders of copper-substituted nickel manganite, Ni1-xCuxMn2O4 ($0 \leq x \leq 1$), were synthesized using the sol-gel auto-combustion technique. Thermal analysis through TG-DTA provided insights into phase formation temperatures. X-ray diffraction (XRD) revealed that the synthesized compounds exhibit a uniform cubic phase. Scanning electron microscopy (SEM) hinted nanosized morphology and transmission electron microscopy (TEM) further confirmed that the particles are nanosized, with an average diameter of 50 nm. The energy-dispersive X-ray spectroscopy (EDS) results were in excellent agreement with the theoretical composition, affirming the successful synthesis of the target material. The gas responses of sintered materials were tested by exposing the films of sintered material to various gases like LPG, NH3, CO2 H2S, Cl2 and ethanol vapours. Evaluations demonstrated that the sensor with x = 0.25 exhibited remarkable selectivity and sensitivity toward ammonia (NH3) at a concentration of 3.33 ppm. This study underscores the exceptional potential of nanosized manganite materials for the sensitive detection of ammonia vapors, addressing a critical environmental and industrial challenge.

1. Introduction

21st century has witnessed unprecedented growth in industrialization globally. This expansion has brought significant economic benefits, including increased production, job creation, and technological advancement. However, it also poses challenges such as environmental degradation, resource depletion, and socio-economic disparities. Balancing industrial progress with sustainability and equitable development is crucial for a resilient future. The release of gases like CO, CO_2, Cl_2, NH_3, ethanol vapors, and H_2S is associated with various industrial processes and activities which are essential for current day to day life of human being. [1] The gases CO, CO_2, Cl_2, NH_3, ethanol vapors and H_2S each pose significant risks to biota. CO impairs oxygen transport in animals and contributes to broader environmental pollution affecting plant health. Elevated CO_2 can enhance plant growth but also drives climate change, which disrupts ecosystems. Chlorine gas causes respiratory issues in animals and damages plant tissues, while ammonia can lead to respiratory problems in animals and soil acidification affecting plant growth. Ethanol vapors are toxic to both animals and plants, impairing growth and health. Hydrogen sulfide is highly toxic to animals and detrimental to plant health, affecting growth and soil quality. Collectively, these gases contribute to environmental degradation, impacting health and biodiversity across ecosystems. [2] Various oxidizing and reducing gases like CO, CO_2, Cl_2, NH_3, ethanol vapours, H_2S have been liberated from different industrial plants as well as mines. The concentration of these gases beyond certain limit is hazardous to human being as well as living organism. Hence it is necessary to monitoring toxic industrial gases and vapours. [3]

Spinel materials can be synthesized through various methods like solid-state reaction, sol-gel method, hydrothermal synthesis, solvothermal synthesis and co-precipitation method. Each technique provides unique benefit, such as cost-effectiveness, precise control, high purity, scalability, rapid production, depending on the specific requirements and desired properties of the spinel material. [4] The sol-gel method offers precise control over composition, allowing for the production of highly homogeneous materials with specific properties. It

Journal of Chemical Health Risks

www.jchr.org

JCHR (2019) 9(4), 398-408 | ISSN:2251-6727

requires lower processing temperatures compared to traditional methods, reducing energy consumption and preserving sensitive components. This technique also provides versatility in forming various material types, such as powders and thin films, and often results in high-purity products with enhanced surface areas and porosities. Additionally, the sol-gel process can be scaled up for industrial production, making it both versatile and cost-effective. [5]

Spinel-type oxides with the general formula AB_2O_4 are a crucial category of mixed metal oxides used in gas sensors. These materials have been extensively studied for their ability to detect both oxidizing and reducing gases. Semiconducting mixed metal oxide sensors offer several advantages, including long lifespan, rapid response and recovery times, low cost, a straightforward electronic structure, and minimal maintenance. [6] These features contribute to their strong commercialization prospects and market potential. [7] Compared to other gas sensor technologies, semiconductor sensors are distinguished by their affordability, high applicability, and reliability, making them accessible and practical for real-time control systems. Recent advancements have highlighted mixed metal oxide spinels as effective materials for gas sensing applications. [8-10] Additionally, composite oxides such as spinels [12] and perovskites [13] have recently been found to be more advantageous than single-metal oxides due to their enhanced selectivity and/or sensitivity to specific harmful gases.

Recently, the demand for ammonia sensors has surged across various technologically important fields, including food technology, chemical engineering, medical diagnosis, environmental protection, automotive interior monitoring, and industrial processes. [14] Despite this increased demand, selectivity remains a significant challenge for these sensors. Therefore, there is a continuous need for improved ammonia sensors that offer high gas response, excellent selectivity, rapid response and recovery times, and long-term stability. It is well-established that the electrical resistivity of semiconducting oxides can be altered by the adsorption of gases. This characteristic has been effectively utilized in semiconductor sensors for detecting both flammable and toxic gases. [15-18]

To address ecological challenges and develop an effective gas sensor for harmful ammonia gas, nanosized copper-substituted nickel manganite was synthesized using the sol-gel technique. This method is favored for its simplicity, cost-effectiveness, and accuracy in fabricating copper-substituted nickel manganites. The material's formation was characterized using advanced analytical techniques. Subsequently, its gas-sensing response to various hazardous gaseous contaminants was measured, with the goal of designing an ideal catalyst for detecting ammonia and reducing health risks in the environment.

2. Experimental Details

2.1 Synthesis of $Ni_{1-x}Cu_xMn_2O_4$ compositions

The nanocrystalline mixed metal oxide system $Ni_{1-x}Cu_xMn_2O_4$ (where x = 0.0, 0.25, 0.5, 0.75and 1.0) was prepared by sol-gel auto combustion method. Analytical grade nickel nitrate [$Ni(NO_3)_2.6H_2O$], copper nitrate [$Cu(NO_3)_3.3H_2O$], manganese nitrate [$Mn(NO_3)_2.4H_2O$], and citric acid [$C_6H_8O_7.H_2O$] were used to prepare system compositions. Metal nitrates and citric acid were dissolved in minimum quantity of deionized water with 1:1 molar ratio. The pH of the solution was adjusted to about 9.0 to 9.5 using ammonia solution. The solution was transformed to dry gel on heating to 353 K. On further heating the dried gel converts in a self-propagating combustion manner untill all the gel completely converted to a floppy powder. The as prepared powder was subjected to thermal analysis for phase temperature identification. The as-prepared precursor powder was pre-sintered at 673 K for 1 h then sintered at 1073 K for 5 h for confirmation of phase formation.

The nanocrystalline mixed metal oxide system $Ni_{1-x}Cu_xMn_2O_4$ (where x = 0.0, 0.25, 0.5, 0.75and 1.0) was prepared using the sol-gel auto-combustion method. The system compositions were synthesized from analytical-grade nickel nitrate nickel nitrate [$Ni(NO_3)_2.6H_2O$], copper nitrate [$Cu(NO_3)_3.3H_2O$], manganese nitrate [$Mn(NO_3)_2.4H_2O$], and citric acid [$C_6H_8O_7.H_2O$]. The metal nitrates and citric acid were dissolved in a minimal amount of deionized water at a 1:1 molar ratio. The pH of the solution was adjusted to approximately 9.0 to 9.5 using ammonia solution. Upon heating to 353 K, the solution gradually transformed into a dry gel. Further heating caused the dried gel to undergo self-propagating combustion until it was entirely converted into a friable powder. The resulting powder was subjected to thermal analysis to identify the phase temperature. The precursor

Journal of Chemical Health Risks

www.jchr.org

JCHR (2019) 9(4), 398-408 | ISSN:2251-6727

powder was then pre-sintered at 673 K for 1 hour and subsequently sintered at 1073 K for 5 hours to confirm phase formation.

2.2 Fabrication of sensor material

The sintered powder was ground using an agate mortar and pestle to achieve a sufficiently fine particle size. A thixotropic paste was then formulated by mixing the resulting fine powder with a solution of ethyl cellulose (a temporary binder) in a blend of organic solvents, including butyl carbitol acetate and terpeneol. The ratio of inorganic to organic components in the paste was maintained at 3:1. This paste was used to prepare thick films, which were applied to a glass substrate using screen printing in the desired patterns. The films were subsequently fired at 500 °C for 4 hours. [19]

The sensing performance of the sensors was examined using a "static gas-sensing system. There were electrical feeds through the base plate. The heat was fixed on the base plate to heat the sample under test up to the required operating temperatures. The current passing through the heating element was monitored using a relay with adjustable ON and OFF time intervals. A Cr-Al thermocouple was used to sense the operating temperature of the sensors. The output of the thermocouple was connected to digital temperature indicators. A gas inlet valve was fitted at one port of the base plate. The required gas concentration inside the static system was achieved by injecting a known volume of test gas using a gas-injecting syringe. A constant voltage was applied to the sensors, and current was measured by a digital Pico-ammeter. Air was allowed to pass into the glass dome after every gaseous exposure cycle.

2.3 Charactrization of synthesized materials

Thermal analysis of the composition, $Ni_{0.5}Cu_{0.5}Mn_2O_4$ was carried out from the TG-DTA analytical method. Stability of the dry citrate complex was checked by scanning the thermogram in the temperature range of 10-1000 °C in static air at the flow rate of 10 °C/ min. Different kinds of thermodynamic and kinetic parameters were determined from the plots of TG-DTA curves.

The phase formation of the sintered copper substituted nickel manganite samples was confirmed by X-ray diffraction studies using Philips PW-1710 X-ray diffractometer with CuKα radiation (λ=1.54178Å).The lattice parameters were calculated for the cubic phase using following relations.

a) For cubic phase $a = d (h^2+ k^2 +l^2)^{1/2}$ -----1

Where, a and c = Lattice parameters, (hkl) = Miller indices

d = interplanar distance

The crystallite size of sintered manganites was calculated from the full width at half maxima of the most intense (311) peak by using Scherrer's formula.

$t = 0.9\lambda/ \beta \cos \theta$ ---------- 2

Where, symbols have their usual meaning.

The X-ray density was calculated according to the formula

$dx = 8M/Na^3$

where,N = Avagadros number (6.023×10^{23} atom/mole)

a = lattice constant which was calculated from the X-ray diffraction pattern. X-ray density is sometimes also called 'theoretical density'.

The FT-IR spectra were recorded in the range of 400 to 1000 cm^{-1} on instrument Perkin Elmer – IR spectrophotometer (model E-2829) in KBr pellets. The SEM micrograph of the samples was obtained using scanning electron microscope (JEOL JSM 6360). The grain size of all the samples was calculated by cottrolls method. Transmission electron microscope (Philips CM 20) was used to evaluate the nanostructure of the typical samples. To study the phase structure of the spinel an SAED pattern of the samples was also taken. Two probe technique was employed to measure the D.C. resistivity of the samples in the temperature range of room temperature to 723 K and specific resistivity was determined using the relation,

$\rho = (\pi d^2 / 4t) R$ ---------- 4

The values of activation energy (eV) were calculated from the plots of log ρ Vs $10^3/T$. Silver paste was applied to both the surfaces of the pellets for good ohmic contacts. The graph of ΔV vs ΔT was plotted and the type of the conduction (n or p type) was evaluated. The thermo-emf measurements were carried out in the temperature range of 300 K to 523 K. Gas sensing

Journal of Chemical Health Risks

www.jchr.org

JCHR (2019) 9(4), 398-408 | ISSN:2251-6727

performances of manganites were tested towards various oxidizing and reducing gases. The electrical resistance of a sensor in dry air is measured by Keithley Autoranging Picoammeter - Cleveland OH with use of conventional circuitry in which the sensor is connected to an external resistor at circuit voltage of 10 V (Aplab 7212 regulated power supplier). The values of device resistor are obtained by monitoring the output voltage across the load resistor. The resistance of the sensor was measured in the presence and absence of the test gas. A known amount of gas was introduced to attain the required level of its concentration. The gas sensing measurements were carried out at different operating temperatures (373 – 623 K). The gas response (S) is defined as the ratio of ΔR, i.e. the change in resistance of the sensor in air (R_a) and in presence of gas (R_g), normalized to the value of sensor resistance in air.

$$(\%)\ S = \left| R_a - R_g \right| / R_a \times 100$$

3. Results and Discussion

3.1. Thermogravimetric analysis

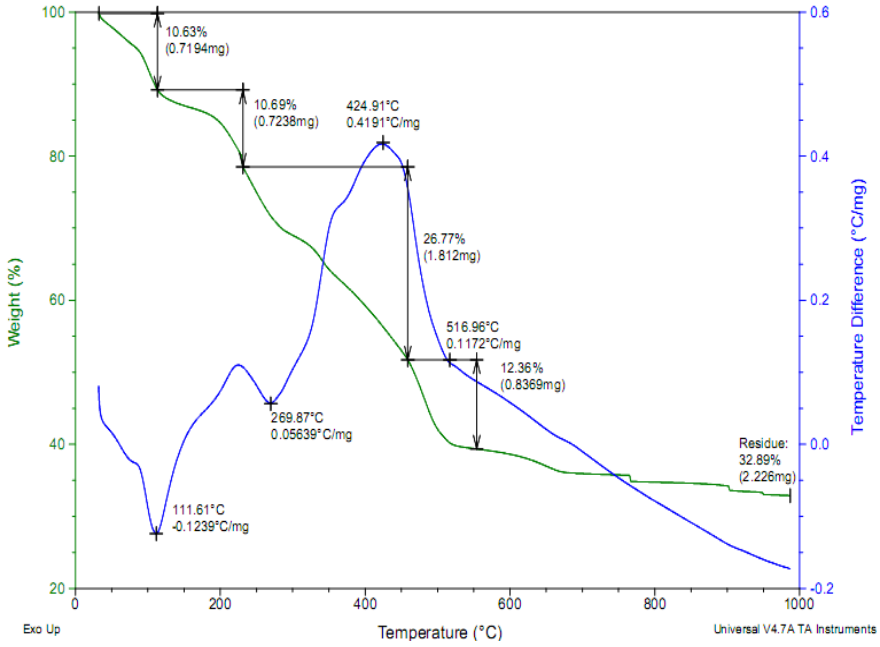

Fig.1 TGA-DTA Spectrum for composition x=0.5 i.e $Ni_{0.5}Cu_{0.5}Mn_2O_4$

Thermogravimetric analysis (TGA) of the precursor with x = 0.5 was conducted from 10 °C to 1000 °C to assess its decomposition behavior, as illustrated in Fig. 1. The sample was placed in a platinum crucible, with ignited alumina used as the reference material, and the heating rate was set to 10 °C min^{-1}. A weight loss of 10.63 % up to 111.61°C corresponds to the release of water and other low-boiling volatile matter, which is supported by a small endothermic peak in the differential thermal analysis (DTA). The second weight loss of 10.69% is attributed to the release of water of crystallization and organic matter. Major weight loss begins at 270 °C and continues until 561°C, indicating significant thermal decomposition of the material due to several key processes that involve major structural breakdowns, ultimately resulting in the formation of the desired mixed metal oxide. A small exothermic peak at 252 °C is associated with the decomposition of impurities, cross linking of polymers, and reactions of residual organic matter. A prominent exothermic peak at 424.91°C corresponds to phase transition. Beyond 800 °C, no further significant weight loss is observed, indicating the phase formation of nickel-substituted copper manganite.

3.2 X-ray diffraction

Journal of Chemical Health Risks

www.jchr.org

JCHR (2019) 9(4), 398-408 | ISSN:2251-6727

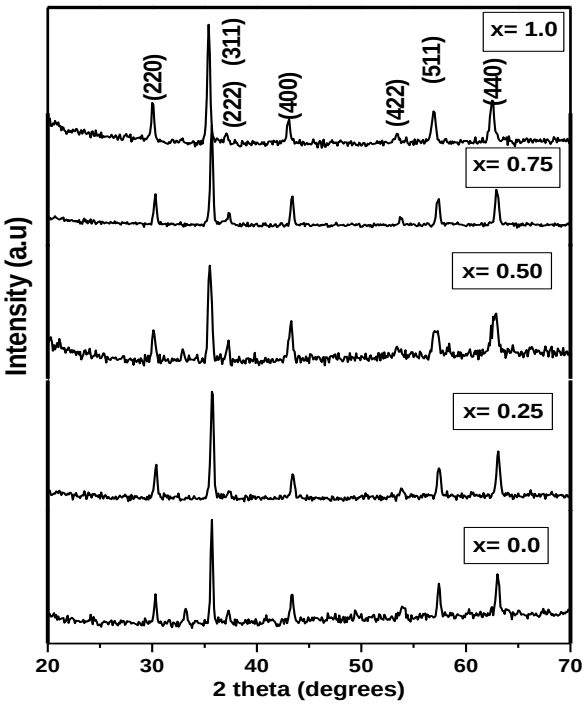

Fig. 2 X-ray diffraction patterns of $Ni_{1-x}Cu_xMn_2O_4$ system

Typical X-Ray diffraction patterns of samples $Ni_{1-x}Cu_xMn_2O_4$ (x= 0.0, 0.25, 0.5, 0.75 and 1.0) obtained by sol gel combustion followed by annealing at 1073 K are shown in Fig. 2 The diffraction pattern for all the manganite samples show cubic spinel structure match well with JCPDS card no. 01-1110 for $NiMn_2O_4$ and JCPDS card no. 34-1400 for $CuMn_2O_4$. [20] The lattice parameters were calculated for the cubic phase. Fig. 3 reveals the linear decreasing trend in the lattice parameter which can be attributed to the replacement of Ni^{2+} (0.78 Å) ion by smaller Cu^{2+}, with ionic radius (0.70 Å), in the system. From the X-ray diffraction peaks, crystallite size was estimated by using Debye Scherrer's formula. [21, 22]

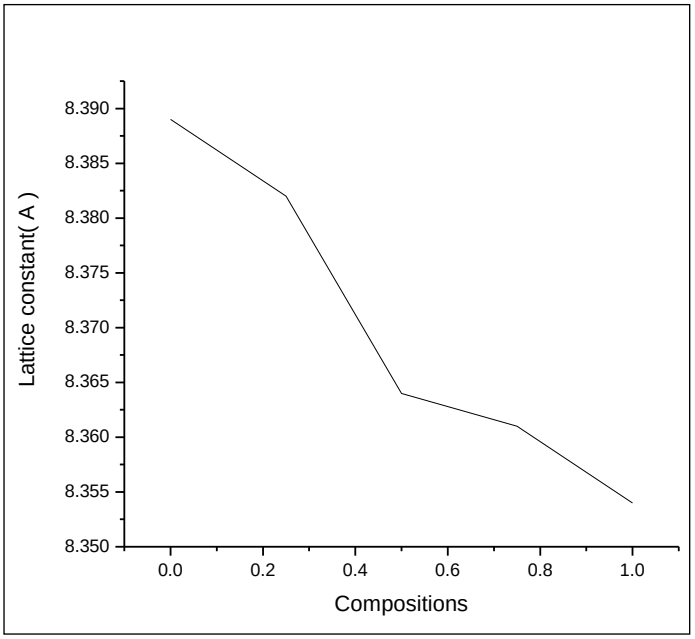

Fig.3 Plot of composition versus lattice constants.

Journal of Chemical Health Risks

www.jchr.org

JCHR (2019) 9(4), 398-408 | ISSN:2251-6727

The values of lattice constant (a), crystallite size (t) and X-ray density (dx) are summarized in Table 1. It is observed that the lattice parameter 'a' decreases with increase in copper content. Crystallite size 't' and X-ray density 'dx' value varies with substitution of copper metal ions.

Composition	Lattice constant 'a', (A^0)	X-ray density, dx (gm/cm^3)	Crystallite size, t (nm)
X=0.0	8.389	5.22	29
X=0.25	8.382	5.27	28
X=0.50	8.368	5.33	28
X=0.75	8.361	5.36	21
X=1.00	8.354	5.39	21

Table.1 Data of lattice parameter, crystallite size, x-ray density, of $Ni_{1-x}Cu_xMn_2O_4$system.

3.3 Scanning Electron Microscopy:

The SEM images of copper-substituted nickel manganites, shown in Fig. 4, reveal that the average grain size across all compositions is around 0.5 μm, attributed to nanoparticle agglomeration. The observed slight increase in grain size with copper substitution suggests an enhanced sintering effect. Furthermore, the addition of copper leads to more pronounced particle agglomeration, indicating that copper influences the microstructural evolution of the manganites.

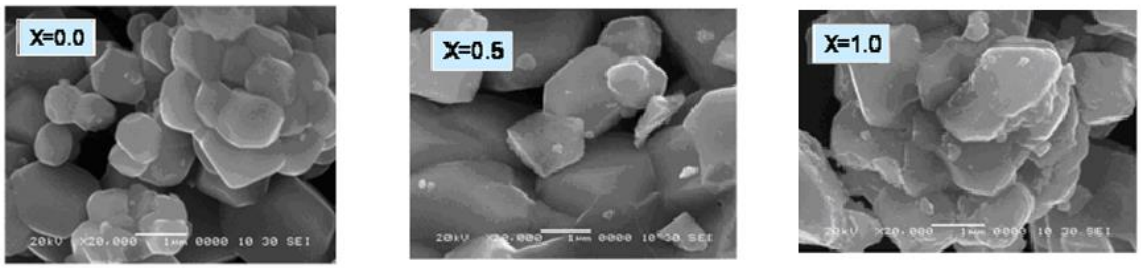

Fig. 4 Typical SEM images for $Ni_{1-x}Cu_xMn_2O_4$ x =0.0, 0.5 and 1.0

3.4 Transmission Electron Microscopy:

A typical TEM image of the $Ni_{0.5}Cu_{0.5}Mn_2O_4$ sample is shown in Fig. 5, confirming that the particles are of uniform dimensions with an average grain size of 50 nm. The Selected Area Electron Diffraction (SAED) pattern of the particles, also presented in Fig. 5, indicates the polycrystalline nature of the individual crystallites and confirms the formation of nanocrystalline spinel manganites.

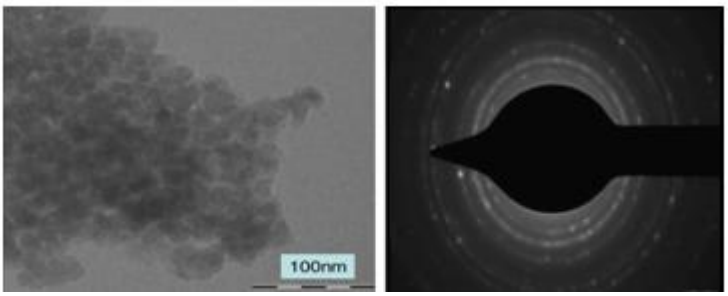

Fig. 5 TEM image and SAED pattern of $Ni_{1-x}Cu_xMn_2O_4$ for x =0.5

3.4 Energy dispersion x-ray analysis:

The composition of the nanocrystalline metal oxides was determined using energy dispersive X-ray analysis (EDAX). The X-ray spectra for compositions x=0.0, x= 0.50 and x= 1.0 are shown in Fig. 6 (a-c). The EDAX spectra confirm the presence of Ni, Mn, Cu, and O in the nanocrystalline material synthesized. Quantitative analysis of the EDAX spectra revealed the relative atomic ratios of the constituents, which closely align

Journal of Chemical Health Risks

www.jchr.org

JCHR (2019) 9(4), 398-408 | ISSN:2251-6727

with the theoretical compositions of $Ni_{1-x}Cu_xMn_2O_4$ system.

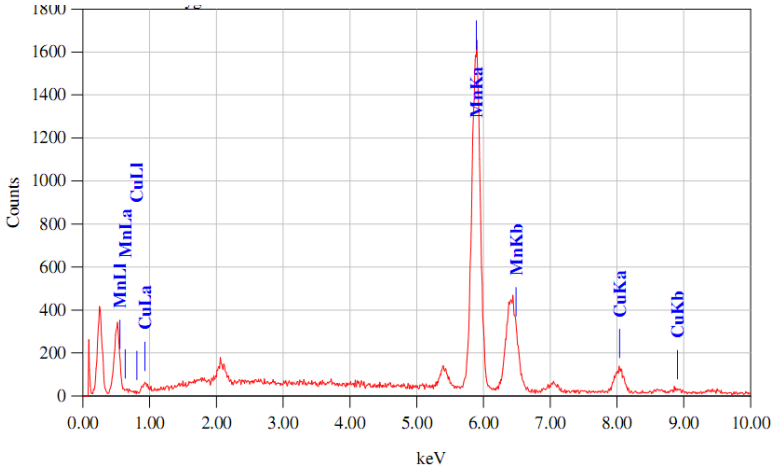

x = 0

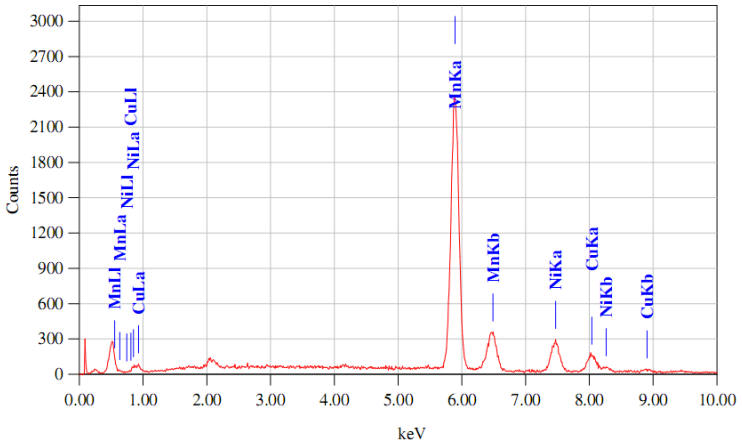

b) x=0.5

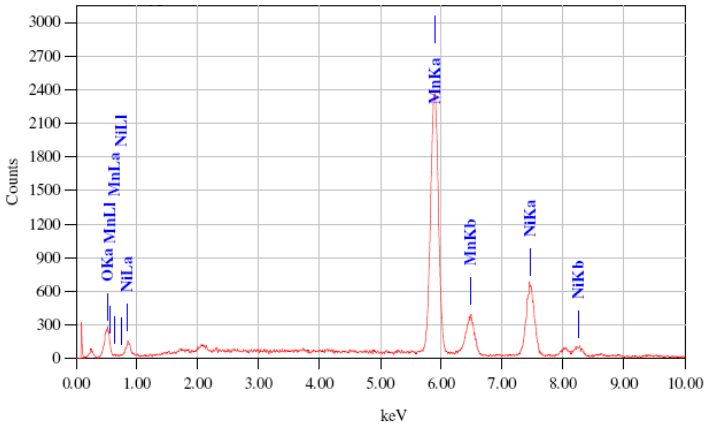

c) x=1.0

Fig.6 (a-c) EDS patterns for the system $Ni_{1-x}Cu_x Mn_2O_4$ samples

Journal of Chemical Health Risks

www.jchr.org

JCHR (2019) 9(4), 398-408 | ISSN:2251-6727

Composition (x)	Atomic % for Element					
	Ni		**Cu**		**Mn**	
	Expt.	Thero.	Expt.	Thero	Expt.	Thero.
X = 0.0	32.08	34.79	--	--	67.92	65.18
X = 0.50	15.31	17.15	16.96	18.58	67.73	64.26
X = 1.0	--	--	33.27	36.63	66.73	63.36

Table.3 Atomic percentage value for the $Ni_{1-x}Cu_xMn_2O_4$System by EDAX analysis

3.5 Electrical resistivity study:

Electrical resistivity of different compositional samples were measured in the range of 10^6 - 10^{10} Ω cm**.** Fig. 7 shows the plots of log ρ vs 1000/T for all the samples which are almost linear without any break indicating their semiconducting nature.

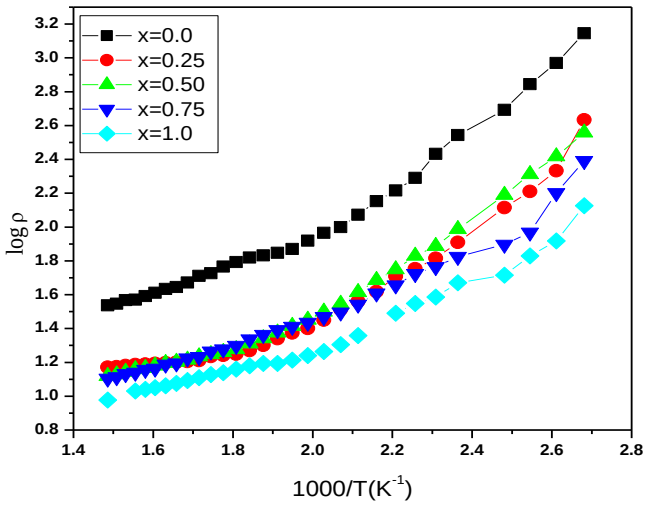

Fig.7 Electrical resistivity study of $Ni_{1-x}Cu_x Mn_2O_4$ system

The relationship $\rho = \rho_o \exp \Delta E/kT$ is found to be obeyed for all compositions. The values of activation energy (ΔE) varied between 0.32 and 0.56 eV which are summarized in Table 4. It can be seen that the resistivity decreases with increasing temperature for all samples. The observed behavior clearly indicates that the present manganites have semiconductor-like behavior. The resistivity is due to the presence of Mn^{2+} ions. The resistivity arises due to the mobility of the extra electron, which comes from Mn^{2+} through the crystal lattice. The movement is described by a hopping mechanism, in which the charge carriers jump from one ionic site to the next. [23] The decrease of the electrical resistivity with increasing temperature may be related to the increase of the drift mobility of thermally activated charge carriers (electron and hole) according to hopping conduction mechanism.

Composition (x)	Activation Energy, ΔE (eV)
0.0	0.32
0.25	0.40
0.5	0.51
0.75	0.54
1.0	0.56

Table No. 4 Energy of activation from resistivity of the samples.

Journal of Chemical Health Risks

www.jchr.org

JCHR (2019) 9(4), 398-408 | ISSN:2251-6727

3.6 Thermoelectric power measurement:

The variations of seebeck coefficient as a function temperature for different composions are shown in Fig. 8. The samples show n-type conductivity**.** The conduction mechanism in n-type specimens is predominantly due to the electrons from Mn^{2+} to Mn^{3+} ions.

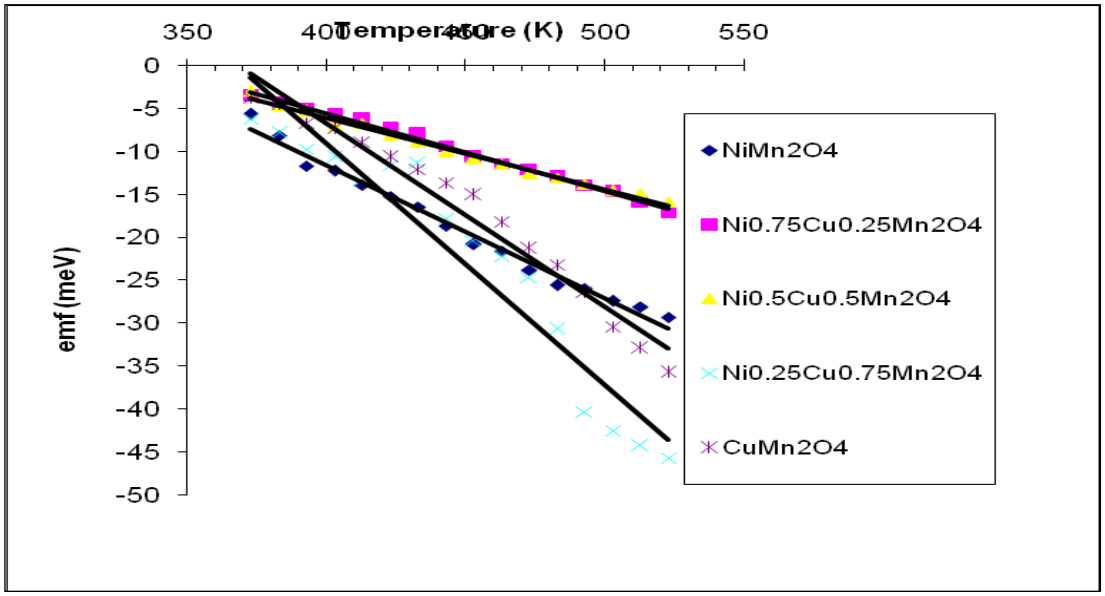

Fig. 8 Thermoelectric power measurement study of $Ni_{1-x}Cu_x Mn_2O_4$ system

3.7 Gas sensing studies:

Gas sensing performance of each composition of the $Ni_{1-x}Cu_xMn_2O_4$ system has been tested for various oxidizing and reducing gases viz. ethanol, LPG, H_2, Cl_2 CO_2 and ammonia gas. The response towards individual gas at elevated temperature is plotted in Fig. 9.

It is seen from the figure that effect of substitution of copper plays a significant role in the detection of various gases at different operating temperatures. It is notable that $Ni_{0.75}Cu_{0.25}Mn_2O_4$ shows remarkable response towards ammonia. Fig. 10 shows response (% S) towards different test gases at 350 °C as the optimum temperature for the gas response. Fig. 11 shows the response of the material increased with increase in ammonia gas concentration. This indicates that, the sensor has large range of detection.

sensing mechanism is predominantly governed by a surface-controlled resistance mechanism. This means that the sensor's resistance changes are primarily determined by the amount and type of chemisorbed oxygen species interacting with the material's surface. However, the reaction process is intricate and involves multiple intermediate steps that are not yet fully elucidated. Understanding these complexities is crucial for optimizing sensor performance and developing more effective gas detection technologies. In gas sensing mechanism, oxygen gets adsorbed on the surface of the sensor at desired operating temperature and electron is transferred from conduction band to adsorbed oxygen atom resulting the formation of ionic species such as O_2^- or $2O^-$. The reaction kinetics may be explained by following reactions, [24]

$$O_{2\,(gas)} \leftrightarrow O_{2(ads)}$$

$$O_2\,(ads) + e^- \leftrightarrow O_2^-$$

$$O_2 + e^- \leftrightarrow 2O^-$$

The electron transfer from the conduction band to the chemisorbed oxygen results in decrease in electron conduction of the sensor. As a consequence, an increase in resistance of the sensor is observed.

The structural c

Journal of Chemical Health Risks

www.jchr.org

JCHR (2019) 9(4), 398-408 | ISSN:2251-6727

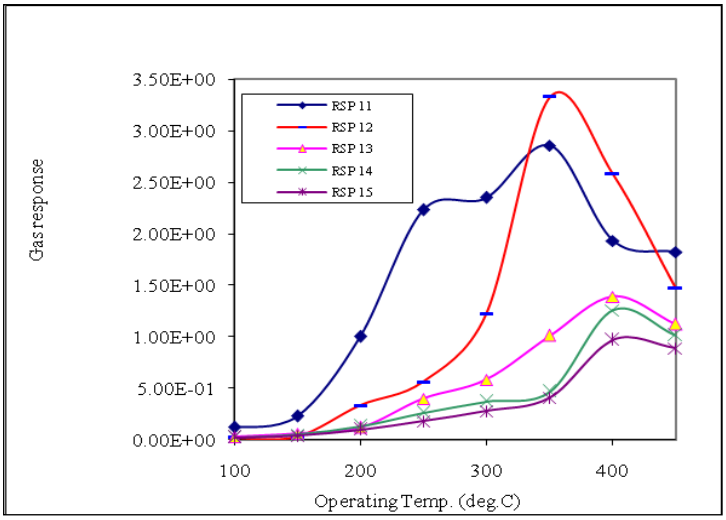

Fig. 9 Gas Response of $Ni_{1-x}Cu_xMn_2O_4$ at different Operating Temperature.

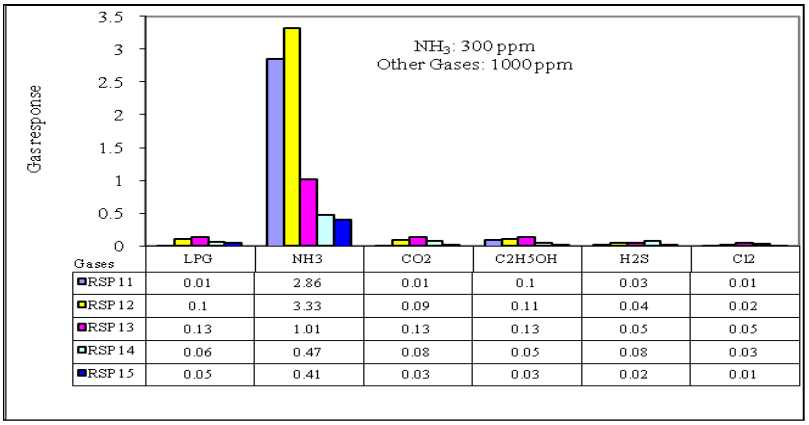

Gases	LPG	NH3	CO2	C2H5OH	H2S	Cl2
RSP11	0.01	2.86	0.01	0.1	0.03	0.01
RSP12	0.1	3.33	0.09	0.11	0.04	0.02
RSP13	0.13	1.01	0.13	0.13	0.05	0.05
RSP14	0.06	0.47	0.08	0.05	0.08	0.03
RSP15	0.05	0.41	0.03	0.03	0.02	0.01

Fig.10 Gas Response of $Ni_{1-x}Cu_xMn_2O_4$ towards different gases.

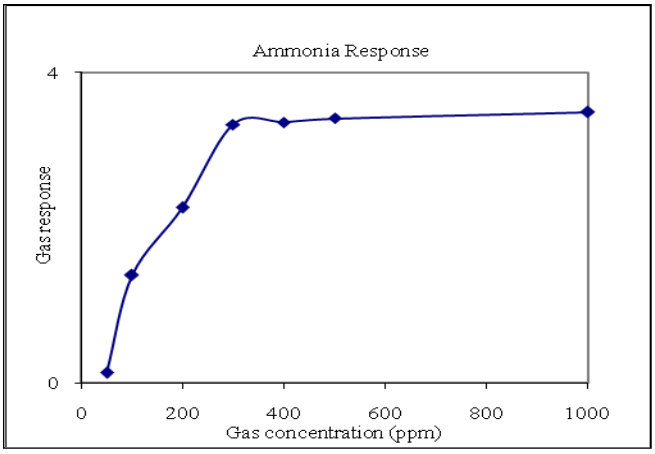

Fig.11 Selectivity of NH_3 gas at different concentrations.

Conclusions

The copper-substituted nickel manganites were synthesized using the sol-gel auto-combustion method, yielding nanocrystalline materials with a distinct cubic phase. The observed reduction in lattice constant is attributed to the smaller ionic radius of copper compared

Journal of Chemical Health Risks

www.jchr.org

JCHR (2019) 9(4), 398-408 | ISSN:2251-6727

to nickel, leading to a structural contraction. Among the synthesized materials, the sensor with (x = 0.25) demonstrated the ultimate performance in gas sensing, exhibiting an exceptional response and selectivity towards ammonia (NH_3) gas. This enhanced performance underscores the material's superior ability to interact with NH_3, making it a highly promising candidate for applications in precise gas detection and environmental monitoring.

References

[1] L. Power, R. K. Tennant, R. T. Jones, Y. Tang, J. Du, A. T. Worsley, J. Love, Sec. Quaternary Science, Geomorphology and Paleoenvironment, volume 6 (2018) https://doi.org/10.3389/feart.2018.0013.

[2] Ghorani-Azam, B. Riahi-Zanjani, M. Balali-Mood, J Res Med Sci. (2016) 21: 65. doi: 10.4103/1735-1995.189646.

[3] Y. Fan, X. Zhu, H . Sui, H. Sun, Z. Wang, Sensors 2019, 19, 369, doi: 10.3390/s19020369.

[4] Q. Zhao, Z. Yan, C. Chen, J. Chen, Chemical Reviews, 117(15) (2017) 10121–10211.

[5] M. Nahrawy, A. A. Soliman, E. M. M. Sakr, H. A. El Attar, Journal of Ovonic Research Vol. 14, No. 3, (2018), 193 – 200.

[6] V. D. Kapse, Res. J. Chem. Sci., Vol. 5(8) (2015) 7-12.

[7] Balamurugan, S. Song, H. Kim, Journal of the Korean Ceramic Society; 55(1) (2018) 1-20.

[8] N. Iftimie, E. Rezlescu, P. D. Popa, N. Rezlescu J. Optoelectronics and Advanced Materials 7 (2005) 911.

[9] Dey, Materials Science and Engineering: B, 229 (2018) 206-217.

[10] J. Zhang, Z. Qin, D. Zeng, C. Xie, Phys. Chem. Chem. Phys., 19 (2017) 6313.

[11] G. F. Fine, L. M. Cavanagh, A. Afonja, R. Binions, Sensors (Basel, Switzerland), 10 (2010) 5469 – 5502.

[12] Šutka, K. A. Gross, Sensors and Actuators B: Chemical Volume 222 (2016) 95-105.

[13] M. Enhessari, A. Salehabadi, Progresses in Chemical Sensor. (2016) doi:10.5772/62559.

[14] Y. Wang, L. Zhang, N. Hu, Y. Wang, Y. Zhang, Z. Zhou, Y. Liu, S. Shen, C. Peng, Nanoscale Research Letters, 9 (2014) 251.

[15] L. Satyanarayana, K. M. Reddey, S. V. Manorama, Sens. Actuators B 89 (2003) 62.

[16] RatnaPhani, S. Manorama, V. J. Rao, Appl. Phys. Lett. 66 (1995) 2619.

[17] Duk-Dong Lee, Dae-Sik Lee, IEEE Sensors 1 (2001) 214.

[18] O. V. Safonova, G. Delabonglise, B. Chenevier, A. M. Gaskov, M. Labeau, J. Mater. Sci. Engg. C 21 (2002) 105.

[19] L. A. Patil and D. R. Patil , Sens. Actuators B, 120 (2006) 316-323.

[20] P.P. Hankare, R.S. Pandav, R.P. Patil, V.T. Vader, K.M. Garadkar, Journal of Alloys and Compounds, Volume 544 (2012) 197-202.

[21] K. M. Shaju, G. V. Subba Rao, B. V. R Chowdari, Solid State Ionics., 69, 15 (2002).

[22] V. Salker, S. M. Gurav, J. Mater. Sci. 35 (2000) 4713.

[23] M. Suzuki, Journal of Physics and Chemistry of Solids, Volume 41, Issue 11(1980) 1253-1260.

[24] Balamurugan and D. W. Lee, Sens. Actuators, B, 192 (2014) 414-422.